Numerical modeling of wave propagation, breaking and run-up on a beach

G.S. Stelling and M. Zijlema

Abstract A numerical method for free-surface flow is presented at the aim of studying water waves in coastal areas. The method builds on the nonlinear shallow water equations and utilizes a non-hydrostatic pressure term to describe short waves. A vertical boundary-fitted grid is used with the water depth divided into a number of layers. A compact finite difference scheme is employed that takes into account the effect of non-hydrostatic pressure with a few number of vertical layers. As a result, the proposed technique is capable of simulating relatively short wave propagation, where both frequency dispersion and nonlinear shoaling play an important role, in an accurate and efficient manner. Mass and momentum are strictly conserved at discrete level while the method only dissipates energy in the case of wave breaking. A simple wet-dry algorithm is applied for a proper calculation of wave run-up on the beach. The computed results show good agreement with analytical and laboratory data for wave propagation, transformation, breaking and run-up within the surf zone.

1 Introduction

Wave transformation in the surf zone plays an important role in coastal engineering since, nearshore waves are the driving forces for many nearshore phenomena, such as longshore currents, water level set-up, sedimentation, erosion, and coastal-structure loading. Surf zones are characterised by the irreversible transformation of organized wave motion of the incident short, wind-generated waves into motions of

G.S. Stelling
Delft University of Technology, Faculty of Civil Engineering and Geosciences, P.O. Box 5048, 2600 GA Delft, The Netherlands, e-mail: g.s.stelling@tudelft.nl

M. Zijlema
Delft University of Technology, Faculty of Civil Engineering and Geosciences, P.O. Box 5048, 2600 GA Delft, The Netherlands, e-mail: m.zijlema@tudelft.nl

different types and scales e.g., turbulence and low-frequency motion (well-known as the ”surf-beat”). The main features associated with the transformation of coastal waves across a surf zone are illustrated in Fig. 1. (SWL denotes the still water level.) In the pre-breaking region, wave transformation is described by the effects of wave

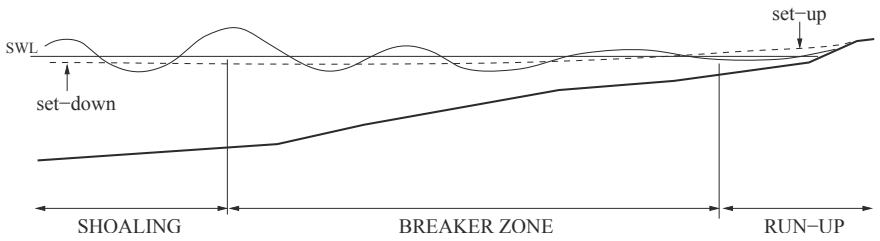

Fig. 1 Wave transformation across a typical surf zone.

steepness due to the nonlinearity (or amplitude dispersion) and wave shortness due to the frequency dispersion. The front face of a wave will steepen continuously until the front becomes vertical. Therefore, the frequency and amplitude dispersion effects must balance each other, so that waves of finite amplitude and permanent form are possible [31]. The bathymetric variations in shallow water distort this balance and cause instabilities and subsequent wave breaking. Once the wave breaks, turbulence is generated and becomes a dominating feature of the flow field. The wavebreaker-generated turbulence balances the steepening of the front and stabilizes the surface profile [31]. The broken waves propagate with a gradual change of form and resemble steady bores. At the end, they become relatively long and run up on the beach. The run-up starts when the bore reaches the shoreline corresponding to a stage of the motion with no water in front of the bore.

The simulation of broken waves and wave run-up amounts to the solution of the nonlinear shallow water (NLSW hereinafter) equations for free-surface flow without viscosity terms in a depth-integrated form [16, 21, 32, 5, 19]. These hyperbolic equations are mathematically equivalent to the Euler equations for compressible flows. Discontinuities are admitted through the weak form of these equations and can take the form of bores which are the hydraulic equivalent of shock waves in aerodynamics. The conservation of energy does not hold across the discontinuities but the conservation of mass and momentum remains valid. By considering the similarity between broken waves and steady bores, energy dissipation due to turbulence generated by wave breaking is inherently accounted for [16, 5].

In the pre-breaking region, however, the NLSW equations do not hold since, they assume a hydrostatic pressure distribution. These equations prohibit a correct calculation of frequency-dispersive or short waves. Moreover, they predict that the front face of any wave or bore will steepen continuously until a vertical front is formed. Only the deviations from hydrostatic pressure can balance the steepening of the front and stabilize the surface profile before it becomes vertical. In this study, we discuss an extension of the NLSW equations to include the effect of vertical

acceleration so that the propagation of short, nonlinear waves with finite amplitudes can be simulated.

A main difficulty occuring in the simulation of free-surface flows is the proper handling of a moving free surface since this is part of the solution itself. Many methods for the treatment of the free surface are described in the literature. The most well-known ones are the Marker-and-Cell (MAC) method [15], the Volume-of-Fluid (VOF) method [18] and the level-set method [30]. An overview of these methods can be found in [25]. Although, these techniques can describe wave overturning in a very accurate manner, they yield more detailed information than necessary for many coastal engineering applications. Moreover, they are too computing intensive when applied to the large-scale wave evolution in the surf zone.

A much simpler approach is the one in which the free-surface motion is tracked using a single-valued function of the horizontal plane as done in the NLSW methodology. Recently, the development of so-called non-hydrostatic models using this approach has been a popular topic of many ocean and coastal modeling activities. Well-known papers on this subject are Casulli and Stelling [9] and Stansby and Zhou [26]. The models in these papers consist of the NLSW equations with the addition of a vertical momentum equation and non-hydrostatic pressure in horizontal momentum equations. As such, the total pressure is decomposed into hydrostatic and non-hydrostatic components. The underlying motivation for this approach is that existing shallow water packages need to be adapted slightly only, since the correction to the hydrostatic pressure is done after the NLSW equations have been solved. As a consequence, this reduces the effort of software extension and maintenance to a minimum. Also, Mahadevan et al. [22] have shown that this technique leads to a more stable and efficient non-hydrostatic calculation than in the case without splitting the pressure into hydrostatic and non-hydrostatic parts. Moreover, the non-hydrostatic models require much fewer grid cells in the vertical direction than the MAC and VOF methods. These benefits make simulations of wave transformation in coastal waters much more feasible and efficient. There is, however, still ongoing research on this approach. The choice of an appropriate numerical approach for a non-hydrostatic free-surface flow model appears to be non-trivial. Several different solution procedures (fractional step versus pressure-correction approach, modeling of the free-surface boundary condition, Cartesian versus $\sigma-$coordinates, etc.) have been proposed by different authors; for an overview, see [35] and the references therein.

Another issue that remains to be discussed is wave breaking. In principle, non-hydrostatic models represent a good balance between nonlinearity (enables wave shoaling) and frequency dispersion (corrects celerity of shoaling wave) so that initiation of the wave breaking process and the associated energy losses can be described adequately by these models. However, most of the well-established non-hydrostatic models, [22, 9, 26], are by no means momentum-conservative. It is evident that the numerical schemes involved must treat shock propagation adequately in order to model broken waves in the surf zone. Traditionally, the shock-capturing schemes applied to shallow water flows at collocated grids are based on the Godunov-type approach, where a discontinuity in the unknown variables (water depth and dis-

charge) is assumed at the cell edges and a Riemann solver is employed to compute the flux across the cell interface [33]. Applications of this approach to the NLSW equations are given e.g., in Ref. [19, 6, 20]. However, this method suffers of four main shortcomings. First, in the case of variable topography, a numerical imbalance may occur, resulting in an artificial flow, caused by inconsistent approximation of the flux-gradients and source terms due to the bottom slope. Secondly, this technique often uses explicit time integration. As a consequence, time steps may be very small due to the CFL condition related to the shallow depth. Thirdly, although, extension to higher dimensions (> 2) by the common local dimensionally split approach is trivial, it is disputable. Finally, extension of the Godunov-type methods to non-hydrostatic flows is non-trivial.

To our knowledge, no papers have been published on the simulation of surf zone phenomena involving breaking waves and wave run-up employing NLSW equations including non-hydrostatic pressure. The reason for this is probably of a historical nature. Traditionally, the effect of non-hydrostatic pressure is taken into account by a Boussinesq-type approximation through adding higher order derivative terms to the NSLW equations [24]. As such, the Boussinesq-type wave models are based on an efficient depth-integrated formulation and have become very popular for real-life applications involving wave dynamics in coastal regions and harbours. One of the main challenges in the development of the Boussinesq-type models is the accurate simulation of wave propagation from deep water through the surf zone. Because such models are strictly valid only for fairly long waves, there have been attempts to improve frequency dispersion that may complicate the underlying formulation. Since then a continual extension of Boussinesq theory has been ongoing with recent advances in its application to highly nonlinear waves and deeper water. See Ref. [11] for a survey of the field. In addition, because of the approximations involved it may not be guaranteed that the Boussinesq-type wave models can predict the onset of wave breaking and its energy losses correctly. It seems that strict energy dissipation can only be proven by adding a dissipation model to the Boussinesq equations; see [11] and the references quoted there.

The purpose of the present work is to report on the experiences that have been gathered in the development of a non-hydrostatic model for coastal waves in the surf zone. We apply an implicit finite difference method for staggered grids as described in [28], originally developed for modeling subcritical flows in, e.g. coastal seas, lakes and estuaries (see, e.g. [27]). The rationale behind this approach is that a discretized form of the NLSW equations can automatically be shock-capturing if the momentum conservation is retained in the numerical scheme. As a consequence, this simple and efficient scheme is able to track the actual location of wave breaking and compute the associated energy dissipation without the aid of analytical solutions for bore approximation or empirical formulations for energy dissipation. In order to resolve the frequency dispersion up to an acceptable level of accuracy using as few layers as possible, a technique as proposed in [29] is employed that is tailored to wave propagation applications. It is based on a compact difference scheme for the approximation of vertical gradient of the non-hydrostatic pressure. Unlike Boussinesq-type wave models, which rely on higher order derivative terms

for better dispersion characteristics, the present model improves its frequency dispersion by increasing the number of vertical layers rather than increasing the order of derivatives of the dependent variables. Hence, it contains at most second order spatial derivatives. Therefore, the second order accurate finite difference approximations are considered to be sufficiently accurate from a numerical point of view. For the calculation of wave run-up on the beach, use of moving boundary conditions is required. Several numerical strategies have been proposed for a proper representation of the interface of water and land. We refer to [1, 7] for overviews on this subject. In the present work, a very simple approach as treated in [28] is adopted. This method tracks the motion of the shoreline very accurately without posing numerical instabilities by ensuring non-negative water depths.

2 Governing Equations

We consider a two-dimensional wave motion in the vertical plane. The waves are assumed to approach perpendicular to the beach. The physical domain represented in a Cartesian coordinate system (x,z) is bounded vertically by the free-surface level above the reference plane, $z = \zeta(x,t)$, and the bottom level measured from the reference plane positively downwards, $z = -d(x)$. Furthermore, t is the time. The water depth is $H = \zeta + d$. See Fig. 2.

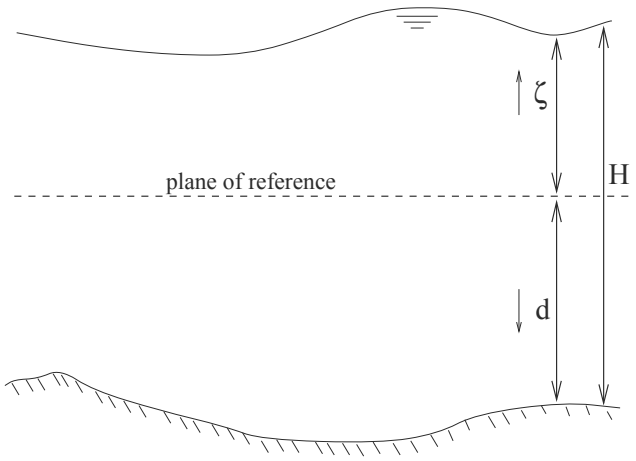

Fig. 2 Water area with free surface and bottom.

The governing equations are the Euler equations for the flow of an incompressible, inviscid fluid with a constant density ρ_0, given by

$$\frac{\partial u}{\partial x} + \frac{\partial w}{\partial z} = 0\,, \tag{1}$$

$$\frac{\partial u}{\partial t}+\frac{\partial u^2}{\partial x}+\frac{\partial wu}{\partial z}+\frac{g}{\rho_0}\frac{\partial \zeta}{\partial x}+\frac{1}{\rho_0}\frac{\partial q}{\partial x}=0\,, \tag{2}$$

$$\frac{\partial w}{\partial t}+\frac{\partial uw}{\partial x}+\frac{\partial w^2}{\partial z}+\frac{1}{\rho_0}\frac{\partial q}{\partial z}=0\,, \tag{3}$$

where $u(x,z,t)$ and $w(x,z,t)$ are the mean velocity components in the horizontal $x-$ and vertical $z-$direction, respectively, g is the acceleration of gravity, $q(x,z,t)$ is the non-hydrostatic pressure. For convenience, we choose $\rho_0=1$. For accuracy reasons, the total pressure has been split into two components, i.e. hydrostatic, $g(\zeta-z)$, and non-hydrostatic, q; for details see, e.g. Ref. [9] and [35]. Next, the kinematic conditions are given by

$$w|_{z=\zeta}=\frac{\partial \zeta}{\partial t}+u\frac{\partial \zeta}{\partial x}\,,\quad w|_{z=-d}=-u\frac{\partial d}{\partial x}\,. \tag{4}$$

To compute the free surface, we integrate Eq. (1) over the water depth H and use the kinematic condition at the free surface (4), giving the following free-surface equation

$$\frac{\partial \zeta}{\partial t}+\frac{\partial Q}{\partial x}=0\,,\quad Q\equiv UH=\int_{-d}^{\zeta}u\,dz \tag{5}$$

with Q the flow rate and U the depth-averaged horizontal velocity.

To get a unique solution, proper numbers and types of boundary conditions are required at all boundaries of the physical domain considered. We distinguish four types of boundaries: i) free surface, ii) bottom, iii) offshore and iv) onshore. In principle, one normal and one tangential component of the velocity and/or stress are imposed at these boundaries. At the free surface, we assume no wind (tangential stress) and $q|_{z=\zeta}=0$ (normal stress). At the bottom, we assume no bottom friction (tangential stress) and the normal velocity is imposed through the kinematic condition (4). Because of continuity, the discharge UH must equal $c_g\zeta$, with c_g the group velocity [11]. For arbitrary depths, we have

$$c_g=n\frac{\omega}{k}\,,\quad n=\frac{1}{2}\left(1+\frac{2kH}{\sinh 2kH}\right)\,, \tag{6}$$

where ω and k are the angular frequency and the wave number, respectively, of the first input harmonic. Thus, we impose the depth-averaged velocity $U=n\omega\zeta/kH$ at the offshore boundary. Finally, we may consider two types of the onshore condition. The moving shoreline, in the case of calculation of wave run-up on the beach, requires a numerical treatment which will be outlined in Sect. 3.2. In the pre-breaking zone, an artificial outflow condition is imposed. Usually, the so-called Sommerfeld radiation condition is employed, which allows the (long) waves to cross the outflow boundary without reflections [11]. This condition is given by

$$\frac{\partial f}{\partial t}+c\frac{\partial f}{\partial x}=0\,, \tag{7}$$

where f represents the surface elevation or the tangential velocity and c is the wave phase velocity equals $c = \sqrt{gH}$ for long waves.

The set of equations (1)−(3), (5) can be considered as mass- and momentum-conservative NLSW equations with the inclusion of the vertical acceleration. These equations are valid in both pre-breaking and breaking regions describing nonlinear shoaling, breaking, dissipation after breaking and run-up of waves.

3 Numerical Framework

The numerical framework is briefly presented and discussed. Distinction is made between space and time discretizations as treated in Sect. 3.1 and 3.2, respectively, after which the solution technique is outlined in Sect. 3.3.

3.1 Space discretization

3.1.1 Grid schematization

The physical domain is discretized by employing a structured grid. A distinction is made between the definition of the grid in the horizontal and vertical direction. In the horizontal planes, we consider a regular grid $\{x_{i+1/2} \,|\, x_{i+1/2} = i\Delta x,\, i = 0,...,I\}$ with Δx the length of the cell. The location of the cell centre is given by $x_i = (x_{i-1/2} + x_{i+1/2})/2$. In the vertical direction, a boundary-fitted grid is employed. The domain is divided into K layers. The interface between two layers is denoted as $z_{k+1/2}(x,t)$ with $k = 0,...,K$. The layer thickness is defined as $h_k = z_{k+1/2} - z_{k-1/2} = f_k H$ with $0 \leq f_k \leq 1$ and $\sum_k f_k = 1$; see Fig. 3. The water level $z_{K+1/2} = \zeta$ and the bottom level $z_{1/2} = -d$ are located at $x = x_i$. As a consequence, $H = \zeta + d$ is given in point i and the water depth at a cell vertex is not uniquely defined. The water depth at $i+1/2$ is denoted as $\hat{H}$ and its approximation depends on the direction of $Q_{i+1/2}$, i.e. the flow rate normal to the face of the water column $i+1/2$, as follows,

$$\hat{H}_{i+1/2} = \begin{cases} H_i\,, & \text{if } Q_{i+1/2} > 0 \\ H_{i+1}\,, & \text{if } Q_{i+1/2} < 0 \\ \max(\zeta_i, \zeta_{i+1}) + \min(d_i, d_{i+1})\,, & \text{if } Q_{i+1/2} = 0 \end{cases} . \tag{8}$$

The approximation of $\hat{H}_{i+1/2}$ in case of $Q_{i+1/2} = 0$ is heuristically based and appears to be very robust. For consistency, we have

$$z_{i+1/2,1/2} = \begin{cases} -d_i\,, & \text{if } Q_{i+1/2} > 0 \\ -d_{i+1}\,, & \text{if } Q_{i+1/2} < 0 \\ -\min(d_i, d_{i+1})\,, & \text{if } Q_{i+1/2} = 0 \end{cases} \tag{9}$$

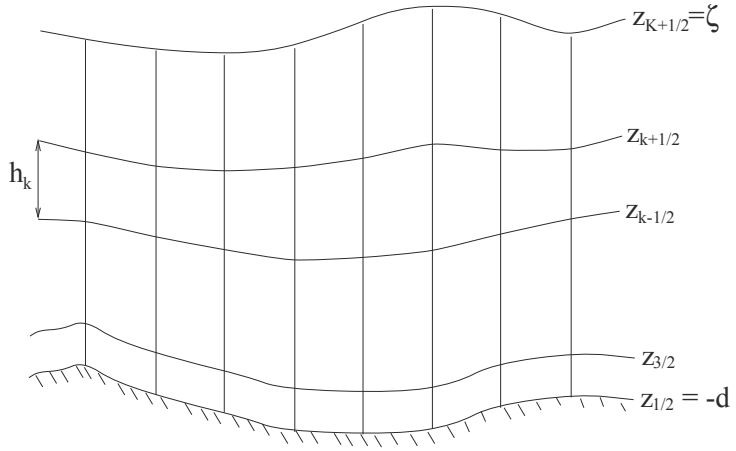

Fig. 3 Vertical grid definition with layer interfaces.

and

$$z_{i+1/2,K+1/2} = \begin{cases} \zeta_i\,, & \text{if } Q_{i+1/2} > 0 \\ \zeta_{i+1}\,, & \text{if } Q_{i+1/2} < 0 \\ \max(\zeta_i, \zeta_{i+1})\,, & \text{if } Q_{i+1/2} = 0 \end{cases} \tag{10}$$

and

$$z_{i+1/2,k+1/2} = z_{i+1/2,k-1/2} + f_k \hat{H}_{i+1/2}\,, \quad k = 1, ..., K-1\,. \tag{11}$$

This completes our description of the grid.

The vertical grid schematization gives rise to the definition of the vertical velocity with respect to the moving layer interfaces. The vertical velocity relative to layer interface $z_{k+1/2}$, denoted as $\omega_{k+1/2}$, is defined as the difference between the vertical velocity along the streamline and the vertical velocity along the interface, as follows,

$$\omega_{k+1/2} = w(z_{k+1/2}) - \frac{\partial z_{k+1/2}}{\partial t} - u(z_{k+1/2}) \frac{\partial z_{k+1/2}}{\partial x}\,. \tag{12}$$

The kinematic boundary conditions, in terms of relative vertical velocity, are $\omega_{1/2} = \omega_{K+1/2} = 0$.

3.1.2 Location of grid variables

A staggered grid arrangement is used in which the velocity components u and w are located at the centers of the cell faces $(i+1/2,k)$ and $(i,k+1/2)$, respectively. The water level ζ is located at i. Concerning the non-hydrostatic pressure q, two ways to assign this unknown to grid points may be employed. This variable can be given either at the cell center (i,k) or at the face $(i,k+1/2)$. The choice depends on the discretization of the vertical pressure gradient, namely, explicit central

differences and an edge-based compact finite difference scheme [17], respectively. Since, the present work deals with the application to wave propagation, only the latter discretization will be considered [29]. The former approximation is particularly meant for applications where vertical structures are important e.g., stratified flows with density currents. Like w, the relative vertical velocity ω is located at the face $(i,k+1/2)$. Fig. 4 shows the staggered grid layout.

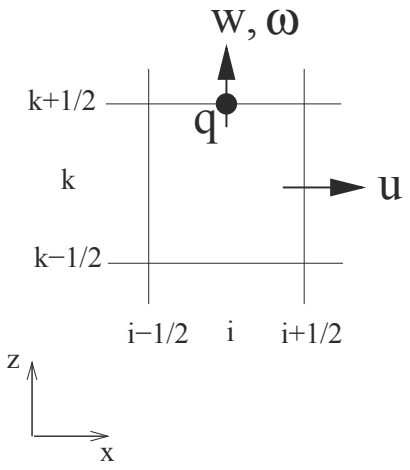

Fig. 4 Arrangement of the unknowns in a staggered grid.

Unknowns not present at points where they are required are computed by interpolation using the fewest number of interpolation points unless stated otherwise. So, $\overline{\varphi}_i^x$ indicates arithmetic averaging of the unknown φ in $x-$direction over their two points of definition that are nearest to i. The unknown φ not given at layer interface $z_{k+1/2}$ is approximated at this interface as

$$\overline{\varphi}^z_{k+1/2} = \varphi(z_{k+1/2}) \approx \frac{\varphi_k h_{k+1} + \varphi_{k+1} h_k}{h_k + h_{k+1}}. \tag{13}$$

Note that $\overline{\varphi}^z_k = (\varphi_{k+1/2} + \varphi_{k-1/2})/2$ since, arithmetic averaging inside a layer is exact. Finally, $\overline{\varphi}^{xz}_{i,k}$ gives the average value of φ at (i,k) resulting from the two one-dimensional interpolation formulas in each direction.

Space discretization of the governing equations is carried out in a finite volume/finite difference fashion. For each unknown, we define a collection of a finite number of non-overlapping control volumes that covers the whole domain. Each unknown, except the water level, is considered as volume-averaged and is at the centre of its control volume,

$$u_{i+1/2,k} = \frac{1}{\hat{h}_{i+1/2,k}} \int_{z=z_{k-1/2}}^{z_{k+1/2}} u|_{x=x_{i+1/2}} dz, \quad w_{i,k+1/2} = \frac{1}{h_{i,k+1/2}} \int_{z=z_k}^{z_{k+1}} w|_{x=x_i} dz,$$
$$q_{i,k+1/2} = \frac{1}{h_{i,k+1/2}} \int_{z=z_k}^{z_{k+1}} q|_{x=x_i} dz \tag{14}$$

with

$$\hat{h}_{i+1/2,k} = f_k \hat{H}_{i+1/2} \tag{15}$$

and

$$h_{i,k+1/2} = \frac{1}{2}(h_{i,k} + h_{i,k+1})\,. \tag{16}$$

3.1.3 Space discretization of global continuity equation

A global mass conservative approximation of Eq. (5) is given by

$$\frac{d\zeta_i}{dt} + \frac{\hat{H}_{i+1/2}U_{i+1/2} - \hat{H}_{i-1/2}U_{i-1/2}}{\Delta x} = 0 \tag{17}$$

with

$$U_{i+1/2} = \frac{1}{\hat{H}_{i+1/2}} \sum_{k=1}^{K} u_{i+1/2,k}\hat{h}_{i+1/2,k}\,. \tag{18}$$

3.1.4 Space discretization of local continuity equation

The space discretization of Eq. (1) consists of two steps. First, this equation is integrated vertically over its control volume and thereafter, an appropriate finite difference scheme is applied to each horizontal term of the equation. The layer-averaged continuity equation (1) for layer $1 \le k \le K$ is obtained using the Leibniz' rule, as follows,

$$\int_{z_{k-1/2}}^{z_{k+1/2}} \left(\frac{\partial u}{\partial x} + \frac{\partial w}{\partial z}\right) dz = \frac{\partial h_k u_k}{\partial x} - u\,\frac{\partial z}{\partial x}\bigg|_{z_{k-1/2}}^{z_{k+1/2}} + w_{k+1/2} - w_{k-1/2} = 0\,. \tag{19}$$

By virtue of (12), this equation becomes

$$\frac{\partial h_k}{\partial t} + \frac{\partial h_k u_k}{\partial x} + \omega_{k+1/2} - \omega_{k-1/2} = 0\,, \tag{20}$$

so that the total amount of water in a moving cell with thickness h_k is conserved. Discretization of Eq. (20) in $x-$direction gives

$$\frac{dh_{i,k}}{dt} + \frac{\phi_{i+1/2,k} - \phi_{i-1/2,k}}{\Delta x} + \omega_{i,k+1/2} - \omega_{i,k-1/2} = 0 \tag{21}$$

with

$$\phi_{i+1/2,k} = \hat{h}_{i+1/2,k} u_{i+1/2,k}\,. \tag{22}$$

3.1.5 Space discretization of horizontal momentum equation

Again, the space discretization of Eq. (2) consists of two steps as outlined in Sect. 3.1.4. The derivation of layer-averaging of the terms in Eq. (2) is given in [35] and will not be repeated here. The layer-averaged $u-$momentum equation in conservative form reads

$$\frac{\partial h_k u_k}{\partial t} + \frac{\partial h_k u_k^2}{\partial x} + \overline{u}^z_{k+1/2}\omega_{k+1/2} - \overline{u}^z_{k-1/2}\omega_{k-1/2} + g h_k \frac{\partial \zeta}{\partial x} + \frac{\partial h_k \overline{q}^z_k}{\partial x} - q_{k+1/2}\frac{\partial z_{k+1/2}}{\partial x} + q_{k-1/2}\frac{\partial z_{k-1/2}}{\partial x} = 0\,. \quad (23)$$

A spatial discretization of Eq. (23) is given by

$$\begin{aligned}
&\frac{d\overline{h}^x_{i+1/2,k}u_{i+1/2,k}}{dt} + \frac{\hat{u}_{i+1,k}\overline{\phi}^x_{i+1,k} - \hat{u}_{i,k}\overline{\phi}^x_{i,k}}{\Delta x} \\
&+\overline{u}^z_{i+1/2,k+1/2}\overline{\omega}^x_{i+1/2,k+1/2} - \overline{u}^z_{i+1/2,k-1/2}\overline{\omega}^x_{i+1/2,k-1/2} \\
&+g\overline{h}^x_{i+1/2,k}\frac{\zeta_{i+1}-\zeta_i}{\Delta x} + \frac{h_{i+1,k}\overline{q}^z_{i+1,k} - h_{i,k}\overline{q}^z_{i,k}}{\Delta x} \\
&-\overline{q}^x_{i+1/2,k+1/2}\frac{z_{i+1,k+1/2}-z_{i,k+1/2}}{\Delta x} + \overline{q}^x_{i+1/2,k-1/2}\frac{z_{i+1,k-1/2}-z_{i,k-1/2}}{\Delta x} = 0\,. \quad (24)
\end{aligned}$$

The one-sided second order upwind scheme is used to approximate $\hat{u}$ at (i,k) [17],

$$\hat{u}_{i,k} = \begin{cases} \frac{3}{2}u_{i-1/2,k} - \frac{1}{2}u_{i-3/2,k}\,, \text{ if } \overline{\phi}^x_{i,k} \geq 0 \\ \frac{3}{2}u_{i+1/2,k} - \frac{1}{2}u_{i+3/2,k}\,, \text{ if } \overline{\phi}^x_{i,k} < 0 \end{cases}\,. \quad (25)$$

This scheme generates a limited amount of numerical dissipation which is sufficient to effectively suppress spurious waves with wavelength $2\Delta x$. These undesired wave components are due to nonlinearities.

Since, the velocity component u is the primitive variable and not $\phi = hu$, Eq. (24) is not appropriate for further implementation. For the reformulation, we first consider the discretized form of Eq. (20) in point $(i+1/2,k)$,

$$\frac{d\overline{h}^x_{i+1/2,k}}{dt} + \frac{\overline{\phi}^x_{i+1,k} - \overline{\phi}^x_{i,k}}{\Delta x} + \overline{\omega}^x_{i+1/2,k+1/2} - \overline{\omega}^x_{i+1/2,k-1/2} = 0\,. \quad (26)$$

Multiplying Eq. (26) with $u_{i+1/2,k}$ and substracting the result from Eq. (24), after which it is divided by $\overline{h}^x_{i+1/2,k}$, yields

$$\frac{du_{i+1/2,k}}{dt}+\frac{1}{\overline{h}^x_{i+1/2,k}}\left(\frac{\overline{\phi}^x_{i+1,k}(\hat{u}_{i+1,k}-u_{i+1/2,k})-\overline{\phi}^x_{i,k}(\hat{u}_{i,k}-u_{i+1/2,k})}{\Delta x}\right)$$
$$+\frac{\overline{\omega}^x_{i+1/2,k+1/2}}{\overline{h}^x_{i+1/2,k}}(\overline{u}^z_{i+1/2,k+1/2}-u_{i+1/2,k})-\frac{\overline{\omega}^x_{i+1/2,k-1/2}}{\overline{h}^x_{i+1/2,k}}(\overline{u}^z_{i+1/2,k-1/2}-u_{i+1/2,k})$$
$$+g\frac{\zeta_{i+1}-\zeta_i}{\Delta x}+\frac{1}{\overline{h}^x_{i+1/2,k}}\left(\frac{h_{i+1,k}\overline{q}^z_{i+1,k}-h_{i,k}\overline{q}^z_{i,k}}{\Delta x}\right)$$
$$-\frac{\overline{q}^x_{i+1/2,k+1/2}}{\overline{h}^x_{i+1/2,k}}\frac{z_{i+1,k+1/2}-z_{i,k+1/2}}{\Delta x}+\frac{\overline{q}^x_{i+1/2,k-1/2}}{\overline{h}^x_{i+1/2,k}}\frac{z_{i+1,k-1/2}-z_{i,k-1/2}}{\Delta x}=0\,. \quad (27)$$

Eq. (27) guarantees conservation of momentum and is thus valid for simulation of breaking waves. Note that Eq. (27) does not contain a bed slope source term. Hence, transition from sub- to supercritical flows near steep bed slopes can be computed correctly.

3.1.6 Space discretization of vertical momentum equation

The final discretized $w-$momentum equation can be derived in exactly the same manner as done for the $u-$momentum equation except for the pressure gradient. The equation is given by

$$\frac{dw_{i,k+1/2}}{dt}+\frac{\overline{\phi}^z_{i+1/2,k+1/2}}{2\overline{h}^z_{i,k+1/2}}\frac{w_{i+1,k+1/2}-w_{i,k+1/2}}{\Delta x}$$
$$+\frac{\overline{\phi}^z_{i-1/2,k+1/2}}{2\overline{h}^z_{i,k+1/2}}\frac{w_{i,k+1/2}-w_{i-1,k+1/2}}{\Delta x}$$
$$+\frac{\overline{\omega}^z_{i,k+1}}{2\overline{h}^z_{i,k+1/2}}(w_{i,k+3/2}-w_{i,k+1/2})+\frac{\overline{\omega}^z_{i,k}}{2\overline{h}^z_{i,k+1/2}}(w_{i,k+1/2}-w_{i,k-1/2})$$
$$+\frac{1}{\overline{h}^z_{i,k+1/2}}\int_{z_k}^{z_{k+1}}\frac{\partial q}{\partial z}|_i dz=0\,. \quad (28)$$

Note that central differences have been used in Eq. (28), i.e.,

$$\hat{w}_{i+1/2,k+1/2}=\frac{1}{2}(w_{i,k+1/2}+w_{i+1,k+1/2})\,. \quad (29)$$

Since, the accuracy of the frequency dispersion for relative short waves strongly depends on the discretization of vertical motion, we apply a second order compact scheme for the approximation of the vertical gradient of non-hydrostatic pressure, allowing very few vertical grid points with relatively low numerical dispersion and

dissipation [17]. Firstly, we consider the $w-$momentum equation at $z_{k+1/2}$, Eq. (28), in which the pressure gradient $\partial q/\partial z$ is approximated through backward differencing and subsequent the $w-$momentum equation at $z_{k-1/2}$ where the approximation of $\partial q/\partial z$ is obtained by means of forward differencing. Thereafter, we take the average of the discretized $w-$momentum equations at $z_{k-1/2}$ and $z_{k+1/2}$ onto the layer k. Thus, the integral of pressure gradient in Eq. (28) is approximated by means of backward differencing,

$$\frac{1}{\overline{h}^z_{i,k+1/2}}\int_{z_k}^{z_{k+1}}\frac{\partial q}{\partial z}|_i dz = \frac{q(z_{i,k+1})-q(z_{i,k})}{\overline{h}^z_{i,k+1/2}} \approx \frac{q_{i,k+1/2}-q_{i,k-1/2}}{h_{i,k}}. \tag{30}$$

The $w-$momentum equation at interface $z_{k-1/2}$ is obtained from Eq. (28) by decreasing the index k by 1. However, the integral of pressure gradient is evaluated using forward differencing. This gives

$$\frac{1}{\overline{h}^z_{i,k-1/2}}\int_{z_{k-1}}^{z_k}\frac{\partial q}{\partial z}|_i dz = \frac{q(z_{i,k})-q(z_{i,k-1})}{\overline{h}^z_{i,k-1/2}} \approx \frac{q_{i,k+1/2}-q_{i,k-1/2}}{h_{i,k}}. \tag{31}$$

Finally, we take the average of the $w-$momentum equations at interfaces $z_{k-1/2}$ and $z_{k+1/2}$, giving

$$\frac{d(w_{i,k+1/2}+w_{i,k-1/2})}{2dt} + \frac{1}{2}\left((L^{\mathrm{w}}w)_{i,k+1/2}+(L^{\mathrm{w}}w)_{i,k-1/2}\right) + \frac{q_{i,k+1/2}-q_{i,k-1/2}}{h_{i,k}} = 0 \tag{32}$$

with L^{w} the discrete operator representing advection terms as outlined before. Due to the use of the compact scheme, Eq. (32) contains two time derivatives for w.

It must be emphasized that Eq. (32) is solved for layers $2 \le k \le K$, i.e. including the free surface, but excluding the bottom. Condition $q|_{z=\zeta} = 0$ can be readily incorporated in Eq. (32) for $k = K$ as $q_{i,K+1/2} = 0$. At the bottom ($k = 1$), the kinematic condition $w|_{z=-d} = -u\partial d/\partial x$ is imposed.

3.2 Time integration

The spatial discretization, explained in the previous section, yields a system of ordinary differential equations as given by Eqs. (17), (21), (27) and (32). For transparency, we summarize the space-discretized momentum equations:

$$\frac{du_{i+1/2,k}}{dt} + (L^{\mathrm{u}}u)_{i+1/2,k} + (G^1_x\zeta)_{i+1/2,k} + (G^2_x q)_{i+1/2,k} = 0 \tag{33}$$

and

$$\frac{d(w_{i,k+1/2}+w_{i,k-1/2})}{dt} + 2(G_z q)_{i,k} + (L^{\mathrm{w}}w)_{i,k+1/2} + (L^{\mathrm{w}}w)_{i,k-1/2} = 0. \tag{34}$$

In Eqs. (33) and (34), the finite difference operators L^{u} and L^{w} are linear and include approximations of the advection terms, whereas G_x^1 and G_x^2 are linear operators representing the gradients in $x-$direction of the water level and non-hydrostatic pressure, respectively. The linear operator G_z refers to the compact scheme for the vertical gradient of the non-hydrostatic pressure within a layer.

For time discretization we use a linear combination of the explicit and implicit Euler method, the so-called $\theta-$method with θ lying between zero and unity. For brevity, we denote $\varphi^{n+\theta} = \theta\varphi^{n+1} + (1-\theta)\varphi^n$ for some quantity φ with n indicating the time level $t^n = n\Delta t$ where Δt is the time step. For $\theta = \frac{1}{2}$ we obtain the second order Crank-Nicolson scheme and for $\theta = 0$ and $\theta = 1$ the first order explicit and implicit Euler schemes are obtained, respectively. For stability, we take $\theta \geq \frac{1}{2}$.

Integration of Eq. (17) in time in a semi-implicit manner yields

$$\frac{\zeta_i^{n+1} - \zeta_i^n}{\Delta t} + \frac{\hat{H}_{i+1/2}^n U_{i+1/2}^{n+\theta} - \hat{H}_{i-1/2}^n U_{i-1/2}^{n+\theta}}{\Delta x} = 0\,. \tag{35}$$

Based on the expressions for $\hat{H}_{i+1/2}$, as given by (8), it can be shown that if the time step is chosen such that $\Delta t|U_{i+1/2}^{n+\theta}|/\Delta x \leq 1$ at every time step then the water depth H_i^{n+1} is non-negative at every time step [28]. Hence, flooding never happens faster than one grid size per time step, which is physically correct. This implies that the calculation of the dry areas does not need any special feature. For this reason, no complicated drying and flooding procedures as described in [27] and [1] are required. For computational efficiency, the momentum equations are not solved and velocities are set to zero if the water depth $\hat{H}_{i+1/2}$ is below a threshold value. For the examples in this study it equals 10^{-5} m.

Eq. (21) is discretised fully implicitly in time, as follows,

$$\frac{h_{i,k}^{n+1} - h_{i,k}^n}{\Delta t} + \frac{\phi_{i+1/2,k}^{n+1} - \phi_{i-1/2,k}^{n+1}}{\Delta x} + \omega_{i,k+1/2}^{n+1} - \omega_{i,k-1/2}^{n+1} = 0\,. \tag{36}$$

Concerning the momentum equations, time discretization takes place by explicit time stepping for advection terms and semi-implicit time stepping using the $\theta-$scheme for both surface level and pressure gradients, as follows,

$$\frac{u_{i+1/2,k}^{n+1} - u_{i+1/2,k}^n}{\Delta t} + (L^{\mathrm{u}}u^n)_{i+1/2,k} + (G_x^1\zeta^{n+\theta})_{i+1/2,k} + (G_x^2 q^{n+\theta})_{i+1/2,k} = 0 \tag{37}$$

and

$$\frac{w_{i,k+1/2}^{n+1} - w_{i,k+1/2}^n}{\Delta t} + \frac{w_{i,k-1/2}^{n+1} - w_{i,k-1/2}^n}{\Delta t} + 2(G_z q^{n+\theta})_{i,k}$$

$$+ (L^{\mathrm{w}}w^n)_{i,k+1/2} + (L^{\mathrm{w}}w^n)_{i,k-1/2} = 0\,. \tag{38}$$

3.3 Solution method

After the spatial and temporal discretization, the both locally and globally mass conserved solution $(\zeta_i^{n+1}, q_{i,k+1/2}^{n+1}, u_{i+1/2,k}^{n+1}, w_{i,k+1/2}^{n+1})$ of Eqs. (35)−(38) is found in two steps. First, the solution $(\zeta_i^{n+1}, u_{i+1/2,k}^{*})$ for hydrostatic flows is obtained with conservation of global mass only. Note that $u_{i+1/2,k}^{*}$ is not the final solution since local mass is not conserved yet. Next, the solution $(q_{i,k+1/2}^{n+1}, u_{i+1/2,k}^{n+1}, w_{i,k+1/2}^{n+1})$ is found such that local mass is conserved. In both steps, a projection method is applied, where correction to the velocity fields for the change in respectively water level and non-hydrostatic pressure is incorporated. The projection method is a well-established predictor-corrector approach for solving the incompressible Navier-Stokes equations and is usually referred to as the pressure correction technique [17].

To find the globally but not necessarily locally mass conserved solution, $U_{i+1/2}^{n+1}$ is replaced by

$$U_{i+1/2}^{*} = \frac{1}{\hat{H}_{i+1/2}^{n}} \sum_{k=1}^{K} \hat{h}_{i+1/2,k}^{n} u_{i+1/2,k}^{*}, \tag{39}$$

and instead of Eq. (35), we now have

$$\frac{\zeta_i^{n+1} - \zeta_i^{n}}{\Delta t} + \frac{\hat{H}_{i+1/2}^{n} U_{i+1/2}^{n+\theta^*} - \hat{H}_{i-1/2}^{n} U_{i-1/2}^{n+\theta^*}}{\Delta x} = 0 \tag{40}$$

with $U^{n+\theta^*} = \theta U^{*} + (1-\theta) U^{n}$. Furthermore, $u_{i+1/2,k}^{*}$ is the solution of the following equation

$$\frac{u_{i+1/2,k}^{*} - u_{i+1/2,k}^{n}}{\Delta t} + (L^{\mathrm{u}} u^{n})_{i+1/2,k} + (G_x^1 \zeta^{n+\theta})_{i+1/2,k} + (G_x^2 q^{n})_{i+1/2,k} = 0\,. \tag{41}$$

Note that Eq. (41) contains the non-hydrostatic pressure at the preceding time level so that u^{*} will not satisfy Eq. (36). Eqs. (40) and (41) are solved using a predictor-corrector procedure as follows. An estimate of the $u^{*}-$velocity, denoted as u^{**}, is made that does not satisfy Eq. (40). This is achieved by means of solving Eq. (41) with the best available guess for the water level,

$$\frac{u_{i+1/2,k}^{**} - u_{i+1/2,k}^{n}}{\Delta t} + (L^{\mathrm{u}} u^{n})_{i+1/2,k} + (G_x^1 \zeta^{n})_{i+1/2,k} + (G_x^2 q^{n})_{i+1/2,k} = 0\,. \tag{42}$$

Next, a correction is computed involving the water level as follows. An expression for u^{*} is obtained by substracting Eq. (42) from Eq. (41), to give

$$u_{i+1/2,k}^{*} = u_{i+1/2,k}^{**} - g\theta\Delta t (G_x^1 \Delta\zeta)_{i+1/2,k} \tag{43}$$

with $\Delta\zeta \equiv \zeta^{n+1} - \zeta^{n}$ the surface level correction. The principle of the projection method is that $\Delta\zeta$ must be such that u^{*} is the solution of Eq. (40) so that mass conservation for each water column is obtained. Multiplying Eq. (43) with $\hat{h}_{i+1/2,k}^{n}$,

summing it from bottom to free surface and substituting into Eq. (40) gives

$$\frac{\Delta\zeta_i}{\Delta t} - \frac{g\theta^2\Delta t}{\Delta x}\left(\hat{H}^n_{i+1/2}(G^1_x\Delta\zeta)_{i+1/2} - \hat{H}^n_{i-1/2}(G^1_x\Delta\zeta)_{i-1/2}\right) =$$

$$-\frac{\theta}{\Delta x}\left(\sum_{k=1}^{K}\hat{h}^n_{i+1/2,k}u^{**}_{i+1/2,k} - \sum_{k=1}^{K}\hat{h}^n_{i-1/2,k}u^{**}_{i-1/2,k}\right)$$

$$-\frac{1-\theta}{\Delta x}\left(\hat{H}^n_{i+1/2}U^n_{i+1/2} - \hat{H}^n_{i-1/2}U^n_{i-1/2}\right). \tag{44}$$

For each point i, we thus have an equation for $\Delta\zeta_i$, $\Delta\zeta_{i-1}$ and $\Delta\zeta_{i+1}$. The resulting tri-diagonal system of equations is solved directly by the Thomas algorithm [17].

Once the water level ζ^{n+1} and the intermediate velocity component u^* are determined, a prediction for the intermediate vertical velocity w^* is computed by using Eq. (38) with the best known non-hydrostatic pressure q^n,

$$\frac{w^*_{i,k+1/2} - w^n_{i,k+1/2}}{\Delta t} + \frac{w^*_{i,k-1/2} - w^n_{i,k-1/2}}{\Delta t} + 2(G_z q^n)_{i,k}$$

$$+(L^{\mathrm{w}}w^n)_{i,k+1/2} + (L^{\mathrm{w}}w^n)_{i,k-1/2} = 0. \tag{45}$$

The computed velocities (u^*, w^*) will not accurately fulfil the local continuity equation (36) and the non-hydrostatic pressure must be corrected to achieve this. The velocities can then be modified accordingly. In deriving an equation for the solution of pressure correction, $\Delta q \equiv q^{n+1} - q^n$, Eqs. (41) and (45) are substracted from Eqs. (37) and (38), respectively, resulting in

$$\frac{u^{n+1}_{i+1/2,k} - u^*_{i+1/2,k}}{\Delta t} + \theta(G^2_x\Delta q)_{i+1/2,k} = 0, \tag{46}$$

$$\frac{w^{n+1}_{i,k+1/2} - w^*_{i,k+1/2}}{\Delta t} + 2\theta(G_z\Delta q)_{i,k} = 0, \tag{47}$$

whereby the difference $w^{n+1}_{i,k-1/2} - w^*_{i,k-1/2}$ is neglected. Based on an analysis, it appears that this neglect does not affect the modeling of linear dispersion [35]. Substitution of Eqs. (46) and (47) into Eq. (36) using expression (12) gives a Poisson equation for Δq,

$$-\frac{\theta\Delta t}{\Delta x}\left(\hat{h}^{n+1}_{i+1/2,k}(G^2_x\Delta q)_{i+1/2,k} - \hat{h}^{n+1}_{i-1/2,k}(G^2_x\Delta q)_{i-1/2,k}\right)$$

$$+\frac{\theta\Delta t\,\partial z^{n+1}_{i,k+1/2}/\partial x}{2\left(h^{n+1}_{i,k} + h^{n+1}_{i,k+1}\right)}\left[h^{n+1}_{i,k+1}\left((G^2_x\Delta q)_{i+1/2,k} + (G^2_x\Delta q)_{i-1/2,k}\right) +\right.$$

$$\left. h^{n+1}_{i,k}\left((G^2_x\Delta q)_{i+1/2,k+1} + (G^2_x\Delta q)_{i-1/2,k+1}\right)\right]$$

$$
\begin{aligned}
&-\frac{\theta\Delta t\partial z^{n+1}_{i,k-1/2}/\partial x}{2\left(h^{n+1}_{i,k-1}+h^{n+1}_{i,k}\right)}\left[h^{n+1}_{i,k}\left((G^2_x\Delta q)_{i+1/2,k-1}+(G^2_x\Delta q)_{i-1/2,k-1}\right)+\right.\\
&\left.h^{n+1}_{i,k-1}\left((G^2_x\Delta q)_{i+1/2,k}+(G^2_x\Delta q)_{i-1/2,k}\right)\right]\\
&-2\theta\Delta t\left[(G_z\Delta q)_{i,k}-(G_z\Delta q)_{i,k-1}\right]=\\
&-\frac{1}{\Delta x}\left(\hat{h}^{n+1}_{i+1/2,k}u^*_{i+1/2,k}-\hat{h}^{n+1}_{i-1/2,k}u^*_{i-1/2,k}\right)\\
&+\overline{u^*_{i,k+1/2}}^{xz}\frac{\partial z^{n+1}_{i,k+1/2}}{\partial x}-\overline{u^*_{i,k-1/2}}^{xz}\frac{\partial z^{n+1}_{i,k-1/2}}{\partial x}\\
&-\left(w^*_{i,k+1/2}-w^*_{i,k-1/2}\right). \qquad (48)
\end{aligned}
$$

Once Δq is obtained, we can calculate $u^{n+1}_{i+1/2,k}$ and $w^{n+1}_{i,k+1/2}$, respectively, through Eqs. (46) and (47). Local mass is conserved.

The matrix of (48) is a non-symmetric discrete Laplacian and contains 15 non-zero diagonals. For the solution, we adopt the BiCGSTAB method [34] preconditioned with the incomplete LU factorizations: ILU [23] and MILU (Modified ILU) [13]. Based on several numerical experiments, an optimum in the convergence rate is found by taking 55% of MILU and 45% of ILU. It has been observed that the pressure correction is slowly time varying. This suggests that there is no need for the system of equations (48) to be preconditioned at every time step. Since preconditioning is relative expensive with respect to amount of work, much CPU-time can be saved by preconditioning the system every ten to twenty time steps, as suggested by our experiments.

The overall solution for a time step can be summarized as follows:

1. Start the sequence by taking the unknowns ζ^n, u^n, w^n, q^n, either initially or from the previous time level.
2. Solve Eq. (42) to obtain u^{**}.
3. Solve Eq. (44) to obtain the correction $\Delta\zeta$ for water level.
4. Correct the water level and horizontal velocity by means of $\zeta^{n+1}=\zeta^n+\Delta\zeta$, Eq. (43) for u^*.
5. Solve Eq. (45) to obtain w^*.
6. Solve the Poisson equation (48) to obtain the correction Δq.
7. Update the non-hydrostatic pressure and velocities using $q^{n+1}=q^n+\Delta q$, Eq. (46) for u^{n+1} and Eq. (47) for w^{n+1}.
8. Update the relative vertical velocity $\omega_{k+1/2}$ from Eq. (12).

4 Numerical Experiments

Our main interest concerns the simulation of transformation of non-linear waves over rapidly varying bathymetry in coastal zones. The present method using the compact scheme is validated by applying it to a number of test cases for which experimental data exist. Concerning the range of applicability of the model to values of kH, indicating the relative importance of linear wave dispersion, results of our numerical analysis, as depicted in Fig. 5, suggest that two layers are sufficient to

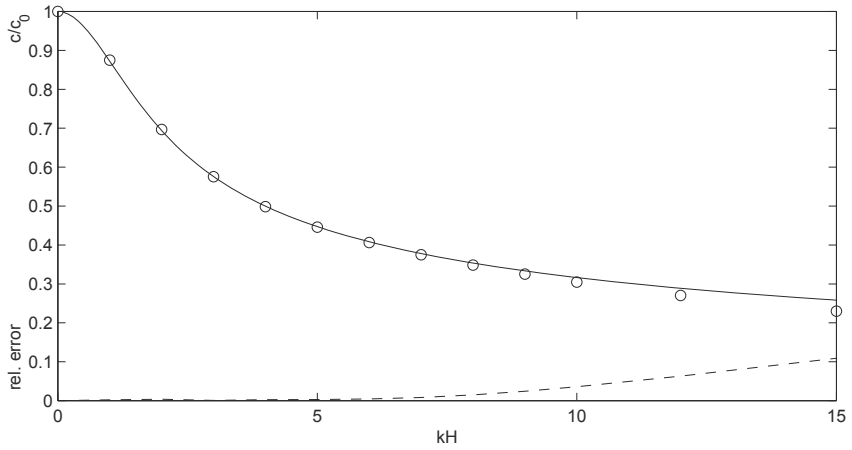

Fig. 5 Normalized wave celerity vs relative depth for linear dispersion. Non-hydrostatic model with two layers (circles), exact (solid line), relative error (dashed line). The quantities $c_0 = \sqrt{gH}$ and c are the long wave celerity and the wave phase velocity, respectively, and the relative error is $|c_{\text{computed}} - c_{\text{exact}}|/c_{\text{exact}}$.

compute linear dispersive waves up to $kH \leq 7$ (typical for coastal areas) with a relative error of at most 1%. Hence, only two equidistant layers are therefore taken in the present numerical experiments.

Simulations of breaking waves and wave run-up are presented in this section. Not only regular waves on a plane sloping bed that are well documented in the literature will be validated but also irregular waves over a barred cross-shore profile. In the test cases discussed, different types of wave breakers for given offshore wave characteristics and beach slope are given, notably, spilling (predominant on flat slopes of beaches) and plunging (predominant on steep slopes) breakers. Details may be found in [12].

While, the cross-shore motion is the main issue in this study, calculation of wave shoaling, refraction and diffraction around a shoal in two horizontal dimensions is also discussed in this section. This relatively computing-intensive application aims among other things at assessing the computational cost per grid point per time step.

The numerical results presented below have been published in previous work; see [29, 35, 36].

4.1 Regular wave breaking on a slope

A number of regular wave experiments on plane slopes were performed by Hansen and Svendsen [14]. The experiments were conducted in a wave flume with a plain slope of 1:34.26. The waves were generated at a depth of 0.36 m. A second order Stokes wave at the toe of the slope is imposed. The wave height is 3.6 cm and the period is 2.0 s. In this case the breaker type is spilling. Time series of the surface elevation were taken at a number of locations along the flume. The simulation period of 120 s has been carried out with a time step of 0.05 s. The first order implicit Euler scheme for time integration is applied ($\theta = 1$). The 15 m flume is covered with 600 grid cells with a gridsize of 0.025 m.

Fig. 6 shows the comparison between the measured and calculated wave height and mean free surface (the slope starts at x=0m). The agreement for wave height is

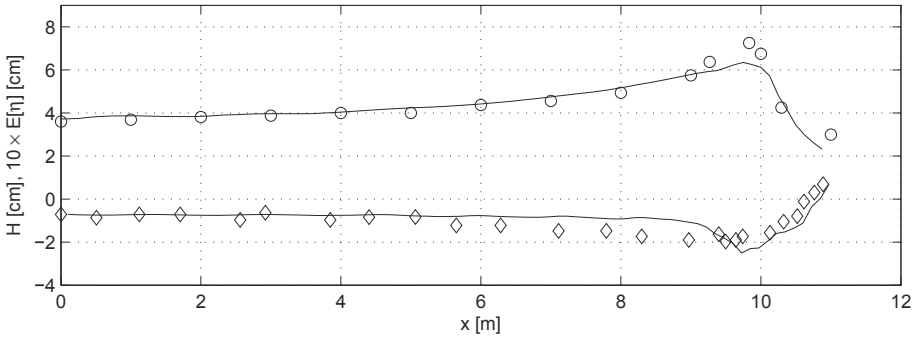

Fig. 6 Computed wave height (upper trend) and set-up (lower trend) compared to data from Hansen and Svendsen [14] for regular spilling breaker. Present method (solid line), experiment (circles, diamonds).

quite good. Also, the model predicts both shoaling and the position of the breaking point correctly. The set-up tends to be underpredicted shoreward of the breaking point. Furthermore, the model could not reproduce the shoreward shift of the set-up relative to the breaking point. These observed deficiencies are believed to be attributed to a relative inaccurate vertical distribution of the horizontal velocity in the breaking zone, since only two layers are adopted here. This may be improved by adding more layers, possibly combined with a turbulence model. Still, with the present model using two layers, the trend of both wave height and set-up is consistently fairly well predicted.

4.2 Periodic wave run-up on a planar beach

An analytical solution for periodic wave run-up on a plane slope by Carrier and Greenspan [8] is used to verify the accuracy of the shoreline movement calculation. This classical test has been used frequently for assessing the quality of various shoreline boundary condition techniques used in the NLSW equations; see e.g., [16, 20].

A sinusoidal wave with height of 0.006 m and period of 10 s is propagating over a beach with slope 1:25. The maximum still water depth is 0.5 m. In the numerical experiment, a grid spacing of Δx=0.04 m and and a time step of Δt=0.05 s is employed. This time step has been chosen so that the water depth is non-negative everywhere. Furthermore, $\theta = 1$ is chosen. The computational flume has a length of 2 incident wavelengths. Only one layer is adopted here. Since, the dispersive effects are relatively small, the non-hydrostatic pressure is not included in the depth-averaged calculation. No wave breaking occurs.

Comparison between the computed free surface envelope and the analytical solution is plotted in Fig. 7. Good agreement is obtained between the computed and

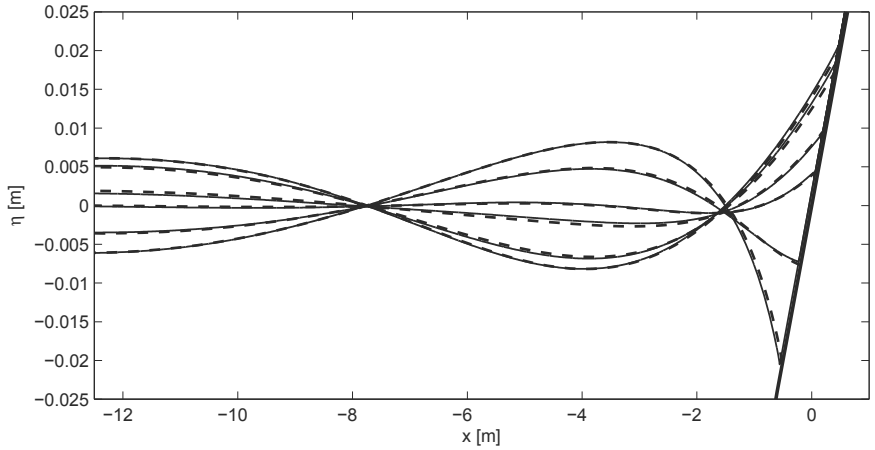

Fig. 7 Computed envelope of surface elevations compared to the analytical solution for the periodic wave run-up on a planar beach. Present method (solid line), theory (dashed line).

theoretical values. This also holds for the horizontal movement of the shoreline as demonstrated in Fig. 8.

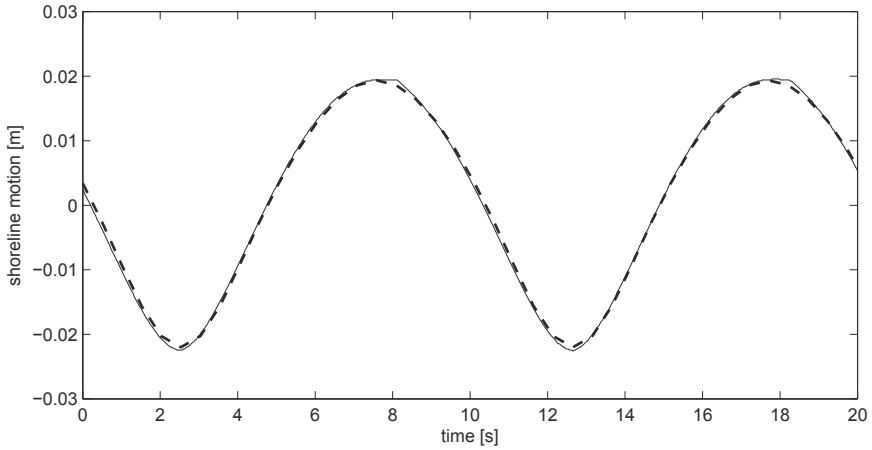

Fig. 8 Computed horizontal shoreline movement compared to the analytical solution for the periodic wave run-up on a planar beach. Present method (solid line), theory (dashed line).

4.3 Regular breaking waves over a submerged bar

In Ref. [10], an overview is given of the physical tests of regular waves over a submerged trapezoidal bar in a wave flume. The description of the experimental set-up for the bar tests can also be found in Ref. [2]. These tests have been used frequently for the evaluation of the performance of various Boussinesq-type wave models. In particular, the bound higher harmonics generated on the upward slope of the bar become free behind the bar, resulting in an irregular wave pattern. This puts heavy demands on the accuracy of the computed dispersion relation. Moreover, contrary to breaking on a slope, the position of incipient wave breaking on the horizontal part of the bar is more difficult to be detected by breaking initiation criteria usually employed in Boussinesq-type models [11].

The computational flume has a length of 30 m. The still water depth is 0.4 m, which is reduced to 0.1 m at the bar. The offshore slope is 1:20 and the shoreward slope is 1:10. The geometry is depicted in Fig. 9 where the regular wave enters from the left (x=0m). Three measurement conditions have been considered in [10] of which one of them is discussed here, namely fairly long wave with a wave period of 2.525 s and a wave height of 2.9 cm. Spilling breakers have been observed in the region between 13.3 m (station 6) and 15.3 m (station 8); see also the snapshot of surface elevation shown in Fig. 9.

In the numerical experiment, a grid spacing of Δx=0.05 m and a time step of Δt=0.01 s is employed. The duration of the simulation is set to 40 s ($\theta = 1$), so that the higher harmonics will reach the farthest station at 21 m before the end of the computation. At the outgoing boundary, the depth at the beach with a slope of 1:25 (starting at x=25 m) has been limited to 0.2 m, so that Sommerfeld radiation condition (7) for long waves can be applied.

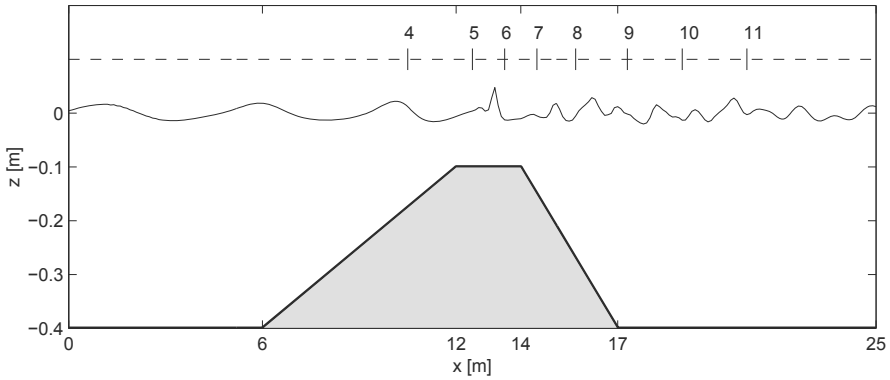

Fig. 9 A snapshot of the free surface and bottom geometry with location of wave gauges for the test of submerged bar.

Comparisons between the measurements and the results of the computations at different locations are plotted in Fig. 10. Good agreement, both in magnitude and phase, is obtained between computed surface elevations and the observed values. It can be seen further that the nonlinear shoaling process is well described by the proposed model. Also, the breaking zone between station 6 and 8, in which wave heights on top of the bar are decreased significantly, is represented well. Finally, the dispersion of the free waves behind the bar is predicted quite well.

4.4 Irregular wave breaking in a laboratory barred surf zone

The laboratory flume test of Boers [4] is considered, in which random, uni-directional waves propagate towards a bar-trough beach profile that was adopted from an actual barred sandy beach (see Fig. 11). The origin of the $x-$axis is at the beginning of the slope. During the experiments, physical parameters in the surf zone such as wave heights and periods have been collected based on the measured free surface elevations at 70 locations. In Ref. [4] a number of wave conditions with different significant wave heights and peak periods for generated incident waves are considered. In this study, a case with a relatively low wave steepness where waves break in the shallow region only is discussed. The breaker type appears to be weakly plunging.

At the offshore boundary, an irregular wave is imposed with the significant wave height of 0.103 m and the peak period of 3.33 s. The grid size is set to 0.025 m and the time step is taken as 0.025 s. The simulation time is set to 1700 s. Since, only permanent waves occur, $\theta = 1$ is chosen for time discretization.

In Fig. 12, spectral comparisons with the numerical and laboratory data are made. The spatial evolution of the wave spectra is characterized by an amplification of spectral levels at both sub- and super-harmonic ranges, consistent with three-wave interaction rules, followed by a transformation toward a broad spectral shape in the

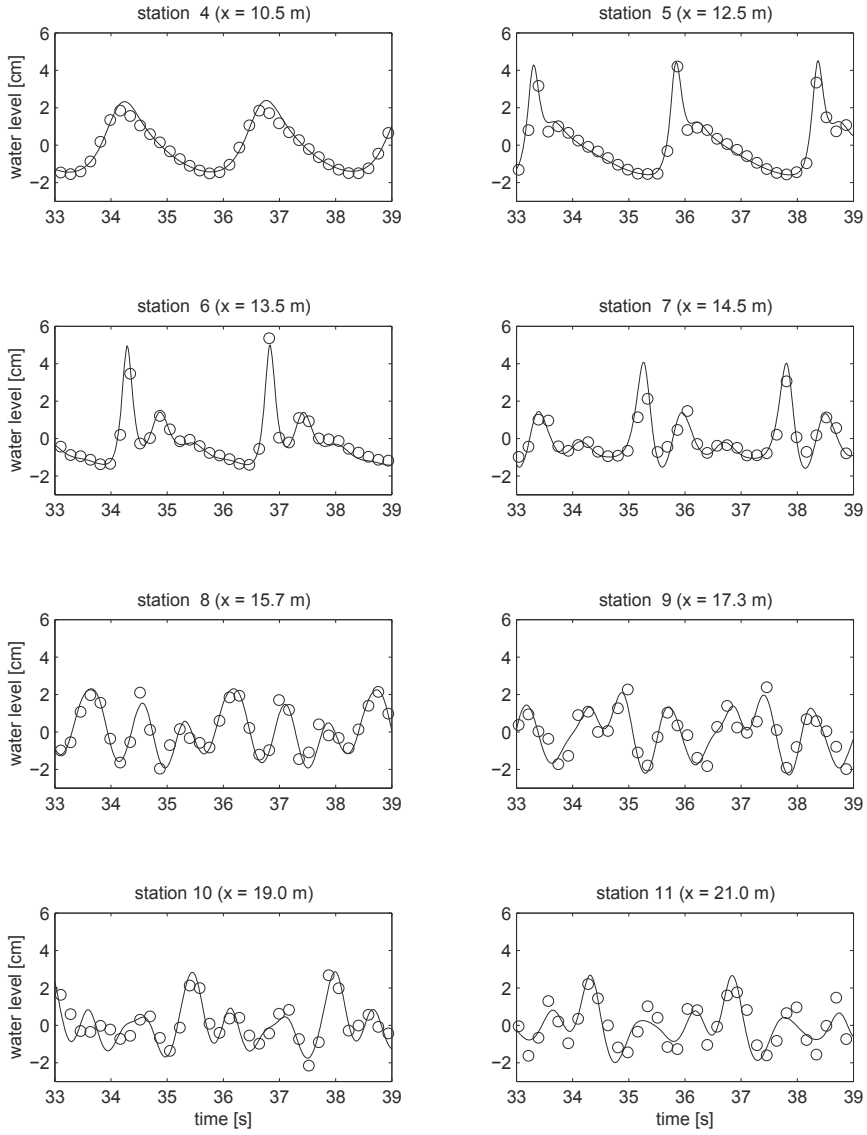

Fig. 10 Computed surface elevations at several stations compared to the measured ones for the wave over submerged bar. Present method (solid line), experiment (circles).

surf zone, attributed to the nonlinear couplings and dissipation. The present numerical method captures the dominant features of the attendant spectral evolution, both in the shoaling region and the surf zone. Nevertheless, from the breaker bar and further, the wave energy is slightly overestimated, in particular the high-frequency part. Apart from this small defect, the numerical model predicts the transforma-

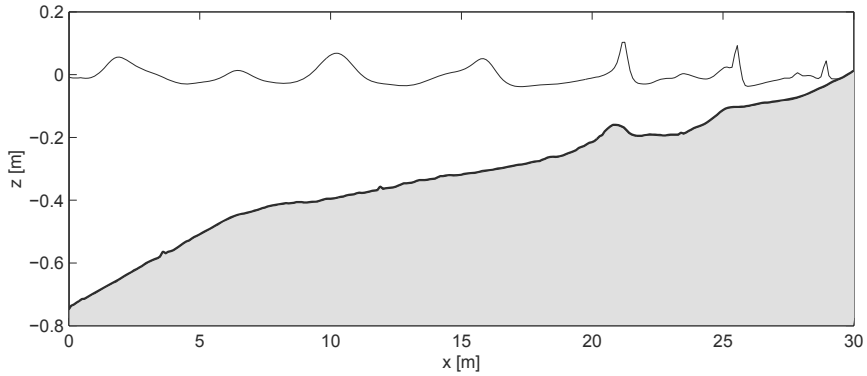

Fig. 11 A snapshot of the free surface and bathymetry of the laboratory flume experiment of Boers [4].

tion of wave energy through the flume where the amount of energy in the short waves reduces, whereas the amount of energy in the long waves increases. Note the slight overestimation of the energy density in the low-frequency part at $x = 26\,\mathrm{m}$ and $x = 28\,\mathrm{m}$, which might be due to the reflection of infragravity waves against the offshore boundary.

4.5 Deformation of waves by an elliptic shoal on sloped bottom

Deformation of waves by a shoal on plane sloping bed is very interesting because of practical importance in the context of surf zone dynamics. From a physical point of view, this wave transformation is challenging, because the waves are ondergoing shoaling, refraction, diffraction and nonlinear dispersion. The experiment conducted by Berkhoff et al. [3] has served as a standard test case for verifying several numerical wave models [11].

The simulations are considered in a rectangle basin $[(x,y) : -10 \le x \le 10, -10 \le y \le 20]$ with a plane slope of 1/50 on which an elliptic shoal is rested; see Fig. 13. Let (x',y') be the slope-oriented coordinates which are related to the (x,y) coordinate system by means of rotation over -20^o. The still water depth without shoal is given in meters by

$$H = \begin{cases} 0.45\,, & \text{for } y' < -5.484 \\ max(0.10, 0.45 - (5.484 + y')/50)\,, & \text{for } y' \ge -5.484 \end{cases}. \tag{49}$$

Instead of shoreline boundary, a minimum depth of 10 cm is employed to prevent breaking waves. The boundary of the shoal is given by

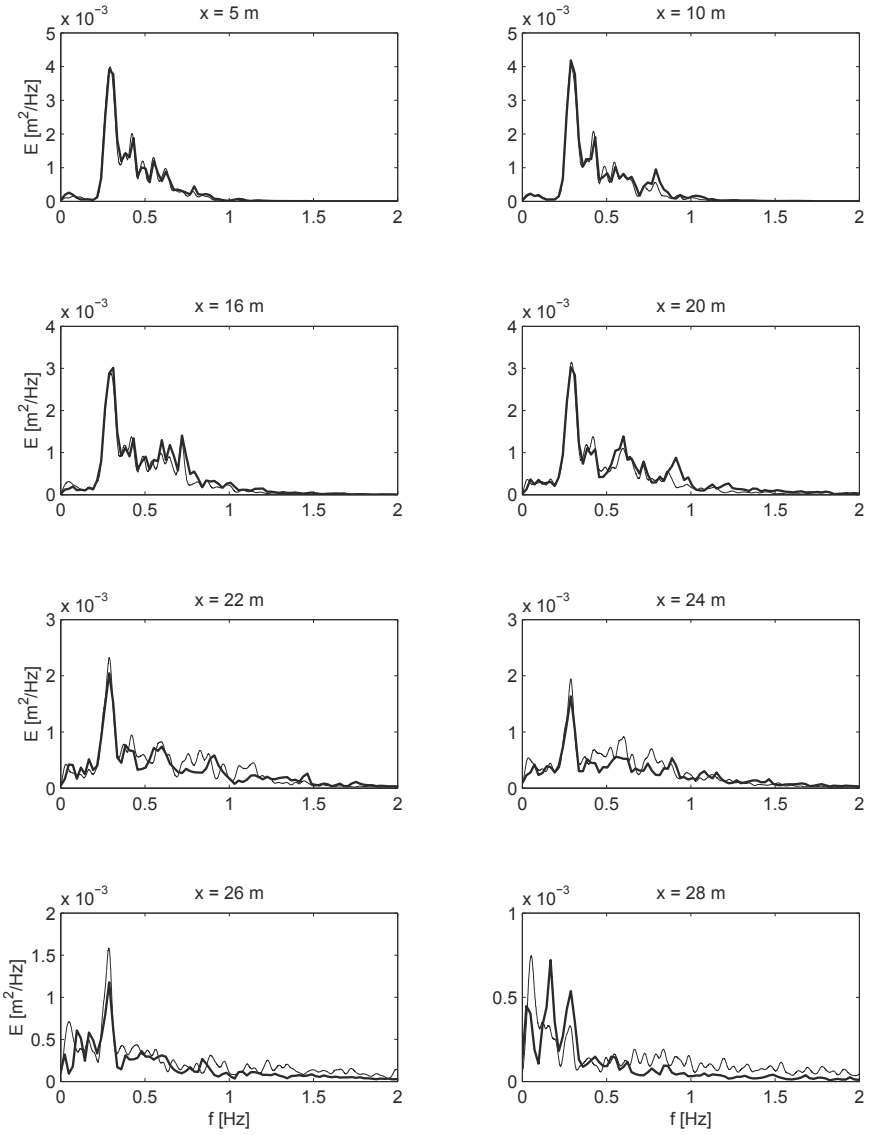

Fig. 12 Computed (thin line) and measured (thick line) energy density spectra at different stations for the irregular wave over bar-trough profile. All spectra use equally spaced frequency intervals and are filtered.

$$\left(\frac{x'}{4}\right) + \left(\frac{y'}{3}\right) = 1\,, \tag{50}$$

whereas the thickness of the shoal is

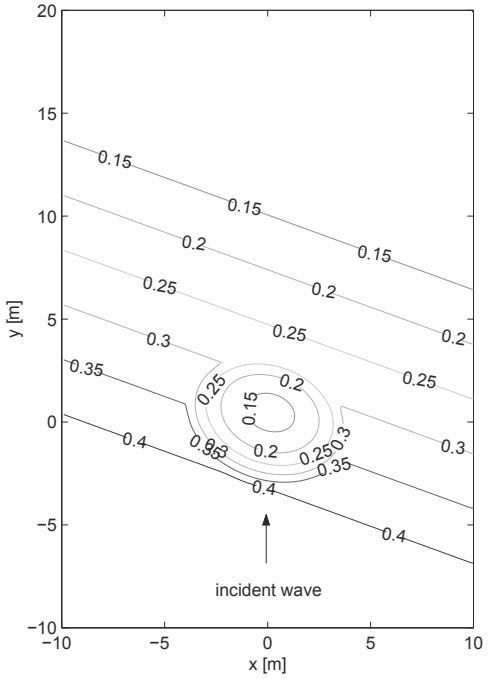

Fig. 13 Bathymetry corresponding to the experiment of Berkhoff et al. [3].

$$d = -0.3 + 0.5\sqrt{1 - \left(\frac{x'}{5}\right)^2 - \left(\frac{y'}{3.75}\right)^2}\,. \tag{51}$$

Monochromatic waves with wave height of 4.64 cm and wave period of 1.0 s are generated at lower boundary $y = -10$ m. The upper boundary, $y = 20$ m, is of the outflow type where Sommerfeld radiation condition (7) is applied. The left and right boundaries are insulated and the free-slip conditions are imposed.

For the present model, the grid size in both directions is set to 0.05 m. The time step is taken as 0.01 s and the simulation period is set to 30 s, so that a steady-state is reached ($\theta = 1$). Since $kH \approx 1.9$ in front of the domain, which is relatively large, only computation with two equidistant layers is carried out.

To get an impression, the computation was carried out on a 64-bit AMD processor (1.8 GHz, 4MB L2 cache) with 4GByte internal memory. Code compilation is achieved using Intel Fortran90 compiler 9.1 with the default optimization. The total CPU time per grid point per time step required was about 20 μs.

Profiles of the computed normalized wave height along four transects, which are the most compelling ones, are given in Fig. 14 and compared with the experimental data. The variation of the waves in cross direction representing the effects of combined refraction and diffraction is predicted fairly well as shown by the comparison of the computed and measured profiles along sections 2 and 5. The comparison

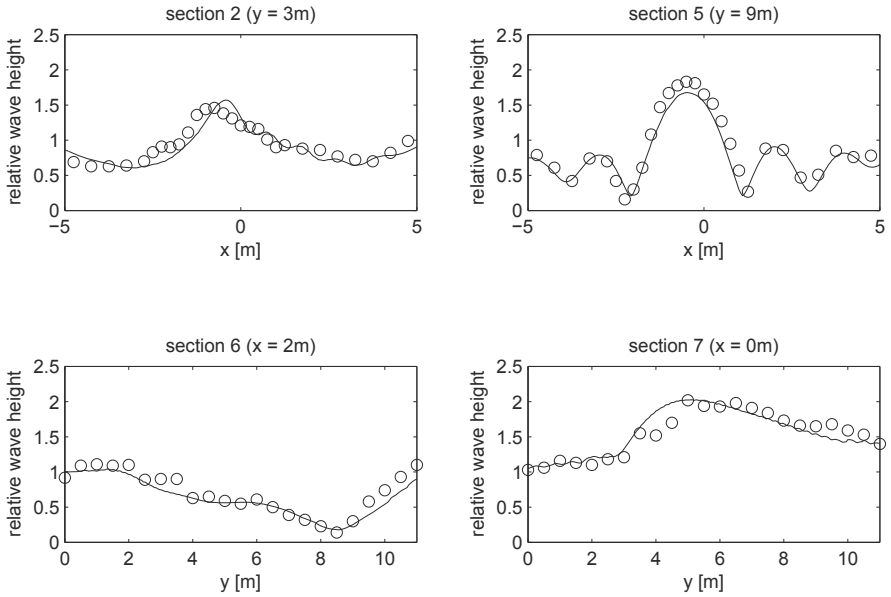

Fig. 14 Computed and measured relative wave heights along different transects for the wave over elliptic shoal. Present method (solid line), experiment (circles).

along sections 6 and 7 indicates that both shoaling and focussing of waves are very well predicted by the present model.

5 Conclusions

A computational method for calculating the conventional nonlinear shallow water equations, including non-hydrostatic pressure has been presented. For accuracy reasons, the pressure is split-up into hydrostatic and non-hydrostatic parts. In the model presented, the water depth is divided into a number of terrain-following layers and the governing equations are integrated in each layer. Next, the second order compact scheme is applied that enables to approximate short wave dynamics with a very limited number of vertical grid points. Simple (semi-)implicit second order finite differences are employed and are based upon a classical staggered grid. In addition, advection terms in the momentum equations are approximated such as to fulfil a proper momentum conservation, which is crucial for accurate computation of energy losses in a wave breaking process. Initiation and cessation of breaking waves can be described adequately by this method. This model does not require any sort of tunable or empirical parameters. Semi-implicit time stepping is done in combination with projection methods, where correction to the velocity fields for the change in both surface elevation and non-hydrostatic pressure is incorporated.

Finally, the algorithm utilizes a simple and numerically stable procedure yielding non-negative water depths with which an accurate representation of the shoreline motion is obtained.

The present method has been employed to model the main features of surf zone dynamics, such as nonlinear shoaling, breaking of waves and wave run-up with good agreement between predictions and observations. The model can be applied in practical applications that comprise areas with spatial dimensions of the order of 10 to 100 wave lengths, particularly in the vicinity of the coast. In the near future, the model will be coupled to a spectral wave model that can be applied on a scale of the order of 100−1000 wave lengths.

References

1. A. Balzano. Evaluation of methods for numerical simulation of wetting and drying in shallow water flow models. *Coast. Eng.*, 34: 83–107, 1998.
2. S. Beji and J.A. Battjes. Experimental investigation of wave propagation over a bar. *Coast. Eng.*, 19: 151–162, 1993.
3. J.C.W. Berkhoff, N. Booy, and A.C. Radder. Verification of numerical wave propagation models for simple harmonic linear water waves. *Coast. Eng.*, 6: 255–279, 1982.
4. M. Boers. Simulation of a surf zone with a barred beach; Part 1: wave heights and wave breaking. Report no. 96-5, Communication on Hydraulic and Geotechnical Engineering, Delft University of Technology, Delft, 1996.
5. M. Brocchini and D.H. Peregrine. Integral flow properties of the swash zone and averaging. *J. Fluid Mech.*, 317: 241–273, 1996.
6. M. Brocchini, R. Bernetti, A. Mancinelli, and G. Albertini. An efficient solver for nearshore flows based on the WAF method. *Coast. Eng.*, 43: 105–129, 2001.
7. M. Brocchini, I.A. Svendsen, R.S. Prasad, and G. Bellotti. A comparison of two different types of shoreline boundary conditions. *Comput. Meth. Appl. Mech. Engng.*, 191: 4475–4496, 2002.
8. G.F. Carrier and H.P. Greenspan. Water waves of finite amplitude on a sloping beach. *J. Fluid Mech.*, 4: 97–109, 1958.
9. V. Casulli and G.S. Stelling. Numerical simulation of 3D quasi-hydrostatic, free-surface flows. *J. Hydr. Eng. ASCE*, 124: 678–686, 1998.
10. M.W. Dingemans. Comparison of computations with Boussinesq-like models and laboratory measurements. MAST G8-M, Report H1684.12, Delft Hydraulics, Delft, 1994.
11. M.W. Dingemans. *Water wave propagation over uneven bottoms*. World Scientific, Singapore, 1997.
12. C.J. Galvin. Breaker type classification on three laboratory beaches. *J. Geophys. Res.*, 73: 3651–3659, 1968.
13. I. Gustafsson. A class of first order factorization methods. *BIT*, 18: 142–156, 1978.
14. J.B. Hansen and I.A. Svendsen. Regular waves in shoaling water: experimental data. Technical report, ISVA series paper 21, Technical University of Denmark, Denmark, 1979.
15. F.H. Harlow and J.E. Welch. Numerical calculation of time-dependent viscous incompressible flow of fluid with a free surface. *Phys. of Fluids*, 8: 2182–2189, 1965.
16. S. Hibberd and D.H. Peregrine. Surf and run-up on a beach: a uniform bore. *J. Fluid Mech.*, 95: 323–345, 1979.
17. C. Hirsch. *Numerical computation of internal and external flows*. John Wiley and Sons, Chichester, 1990.
18. C.W. Hirt and B.D. Nichols. Volume of fluid (VOF) method for the dynamics of free boundaries. *J. Comput. Phys.*, 39: 201–225, 1981.

19. K. Hu, C.G. Mingham, and D.M. Causon. Numerical simulation of wave overtopping of coastal structures using the non-linear shallow water equations. *Coast. Eng.*, 41: 433–465, 2000.
20. M.E. Hubbard and N. Dodd. A 2D numerical model of wave run-up and overtopping. *Coast. Eng.*, 47: 1–26, 2002.
21. N. Kobayashi, A.K. Otta, and I. Roy. Wave reflection and run-up on rough slopes. *J. Waterw. Port Coast. Ocean Eng.*, 113: 282–298, 1987.
22. A. Mahadevan, J. Oliger, and R. Street. A nonhydrostatic mesoscale ocean model. Part II: numerical implementation. *J. Phys. Oceanogr.*, 26: 1881–1900, 1996.
23. J.A. Meijerink and H.A. Van der Vorst. An iterative solution method for linear systems of which the coefficient matrix is a symmetric M-matrix. *Math. Comput.*, 31: 148–162, 1977.
24. D.H. Peregrine. Long waves on a beach. *J. Fluid Mech.*, 27: 815–827, 1967.
25. R. Scardovelli and S. Zaleski. Direct numerical simulation of free-surface and interfacial flow. *Annu. Rev. Fluid Mech.*, 31: 567–603, 1999.
26. P.K. Stansby and J.G. Zhou. Shallow-water flow solver with non-hydrostatic pressure: 2D vertical plane problems. *Int. J. Numer. Meth. Fluids*, 28: 514–563, 1998.
27. G.S. Stelling. *On the construction of computational methods for shallow water flow problems*. PhD thesis, Delft University of Technology, Delft, 1983.
28. G.S. Stelling and S.P.A. Duinmeijer. A staggered conservative scheme for every Froude number in rapidly varied shallow water flows. *Int. J. Numer. Meth. Fluids*, 43: 1329–1354, 2003.
29. G. Stelling and M. Zijlema. An accurate and efficient finite-difference algorithm for non-hydrostatic free-surface flow with application to wave propagation. *Int. J. Numer. Meth. Fluids*, 43: 1–23, 2003.
30. M. Sussman, P. Smereka and S. Osher. A level set approach for computing solutions to incompressible two-phase flow. *J. Comput. Phys.*, 114: 146–159, 1994.
31. I.A. Svendsen and P.A. Madsen. A turbulent bore on a beach. *J. Fluid Mech.*, 148: 73–96, 1984.
32. V.V. Titov and C.E. Synolakis. Modeling of breaking and nonbreaking long-wave evolution and runup using VTCS-2. *J. Waterw. Port Coast. Ocean Eng.*, 121: 308–316, 1995.
33. E.F. Toro. *Shock-capturing methods for free-surface shallow flows*. John Wiley, New York, 2001.
34. H.A. Van der Vorst. Bi-CGSTAB: a fast and smoothly converging variant of Bi-CG for the solution of nonsymmetric linear systems. *SIAM J. Sci. Stat. Comput.*, 13: 631–644, 1992.
35. M. Zijlema and G.S. Stelling. Further experiences with computing non-hydrostatic free-surface flows involving water waves. *Int. J. Numer. Meth. Fluids*, 48: 169–197, 2005.
36. M. Zijlema and G.S. Stelling. Efficient computation of surf zone waves using the nonlinear shallow water equations with non-hydrostatic pressure *Coast. Eng.*, doi:10.1016/j.coastaleng.2008.02.020, 2008.